Prepared for submission to JHEP

# Measurement of energy flow, cross section and average inelasticity of forward neutrons generated in $\sqrt{s} = 13$ TeV proton-proton collisions with the LHCf Arm2 detector



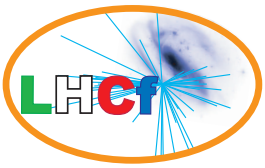



## The LHCf collaboration

O. Adriani,[a,b] E. Berti,[a,b,1] L. Bonechi,[a] M. Bongi,[a,b] R. D'Alessandro,[a,b] S. Detti,[a] M. Haguenauer,[c] Y. Itow,[d,e] K. Kasahara,[f] H. Menjo,[d] Y. Muraki,[d] K. Ohashi,[d] P. Papini,[a] S. Ricciarini,[a,g] T. Sako,[h] N. Sakurai,[i] K. Sato,[d] T. Tamura,[j] A. Tiberio,[a,b] S. Torii,[k] A. Tricomi,[l,m] W.C. Turner,[n] M. Ueno[d]

[a] *INFN Section of Florence, Florence, Italy*
[b] *University of Florence, Florence, Italy*
[c] *Ecole-Polytechnique, Palaiseau, France*
[d] *Institute for Space-Earth Environmental Research, Nagoya University, Nagoya, Japan*
[e] *Kobayashi-Maskawa Institute for the Origin of Particles and the Universe, Nagoya University, Nagoya, Japan*
[f] *Faculty of System Engineering, Shibaura Institute of Technology, Tokyo, Japan*
[g] *IFAC-CNR, Florence, Italy*
[h] *Institute for Cosmic Ray Research, University of Tokyo, Chiba, Japan*
[i] *Tokushima University, Tokushima, Japan*
[j] *Kanagawa University, Kanagawa, Japan*
[k] *RISE, Waseda University, Shinjuku, Tokyo, Japan*
[l] *INFN Section of Catania, Italy*
[m] *University of Catania, Catania, Italy*
[n] *LBNL, Berkeley, California, USA*

*E-mail:* eugenio.berti@fi.infn.it

[1] Corresponding author.

Abstract: In this paper, we report the measurement of the energy flow, the cross section and the average inelasticity of forward neutrons (+ antineutrons) generated in $\sqrt{s} = 13$ TeV proton-proton collisions. These quantities are obtained from the inclusive differential production cross section, measured using the LHCf Arm2 detector at the CERN Large Hadron Collider. The measurements are relative to six pseudorapidity regions: three of them ($\eta > 10.75$, $8.99 < \eta < 9.21$ and $8.80 < \eta < 8.99$) were already published in another work, whereas the remaining three ($10.06 < \eta < 10.75$, $9.65 < \eta < 10.06$ and $8.65 < \eta < 8.80$) are considered here for the first time. The analysis was carried out using a data set acquired in June 2015 with a corresponding integrated luminosity of 0.194 nb$^{-1}$. Comparing our results with the expectations of several hadronic interaction models used to simulate cosmic ray air showers, we found that none of these generators has a satisfactory agreement in all the phase space selected for the analysis. Regarding the inclusive differential production cross section, no model is able to qualitatively or quantitatively reproduce the experimental measurements in $\eta > 10.76$, whereas, at lower pseudorapidity, the results indicate a still significant but less serious deviation. In this last case, depending on the pseudorapidity region, the generator showing the best overall agreement with data is either SIBYLL 2.3 or EPOS-LHC. Regarding the other quantities derived from these distributions, the observed energy flow and cross section are well reproduced by EPOS-LHC, apart from the most forward region. On the other side, the average inelasticity measured by our experiment is compatible with QGSJET II-04 predictions only, even if no generator has a satisfactorily agreement with the observed elasticity distribution. All these results indicate that, even considering post-LHC models, there is still a significant discrepancy between generators and data, emphasizing the benefit that all models would have from a tuning that takes into account the LHCf measurements relative to forward neutron production.

Keywords: LHCf, Large Hadron Collider, Hadronic Interaction Models, Ultra High Energy Cosmic Rays, Extensive Air Showers, Forward Leading Baryon, Energy Flow, Cross Section, Average Inelasticity, Neutron

## Contents



## 1 Introduction

In the last decade, thanks to the large statistics obtained by gigantic cosmic ray air shower experiments like the Pierre Auger Observatory [1] and the Telescope Array [2], various theories have been suggested to explain the mechanisms responsible for the acceleration and propagation of the ultra-high energy cosmic rays, *i.e.* cosmic rays with energies above $10^{18}$ eV [3]. In order to shed light on their origin, the mass composition is a key observable, but its determination is challenging because it relies on the comparison with air shower simulations where a hadronic interaction model must be assumed. Due to the lack of high-energy calibration data, these generators are affected by large differences among them, which in turn constitute the major uncertainty on mass composition measurements [4]. In order to reduce this systematic contribution, we need accurate information on several parameters used to model the development of the extensive air showers, *i.e.* the showers that cosmic rays form when interact in the atmosphere. This information can be extracted from the measurements carried out at hadronic colliders and the CERN Large Hadron Collider (LHC) [5] is the best candidate to accomplish this task. Indeed, during LHC Run II, the machine operated p-p collisions at $\sqrt{s} = 13$ TeV, which is the highest energy ever achieved at a collider and not so distant from the one of ultra high energy cosmic rays (equivalent to the collision of a $0.9 \times 10^{16}$ eV proton with a proton at rest).

The main parameters connected to air shower development are: inelastic cross section, multiplicity of secondaries and forward energy distributions, from which we can derive the average inelasticity. At LHC, the former two quantities are mainly accessible to the four central detectors and roman pot detectors like TOTEM [6] and ATLAS ALFA [7], whereas the latter two quantities can be measured only by dedicated forward detectors. Some of the results obtained in LHC Run I from the first group of experiments (*e.g.* [8–11]) were used to tune the so-called post-LHC models, like QGSJET II-04 [12], EPOS-LHC [13] and SIBYLL 2.3 [14]. However, the level of agreement among these models is still far from satisfactory [15], thus indicating the importance of the second group of experiments. At LHC, LHCf [16] is the only experiment that has been specifically designed to accurately measure the distributions of very forward particles produced in hadronic collisions.

Because of the key role that forward baryons have in the development of the atmospheric showers and in the abundance of the muonic component [17], a large activity of the LHCf collaboration is dedicated to neutron measurements. A first result relative to the inclusive differential production cross section of very forward neutrons+antineutrons (hereafter simply called *neutrons*) generated in p-p collisions at $\sqrt{s} = 13$ TeV was already published [18]. Here we extend this analysis from three to six pseudorapidity regions, in order to have enough points to derive three quantities that are directly connected to air shower development: neutron energy flow, cross section and average inelasticity. It is worth mentioning that these are the first measurements of this type at such a high energy and that their direct comparison to generator expectations gives an important indication on the validity of these models for air shower simulation.

## 2 The LHCf experiment

The LHCf experiment consists of two detectors [19], Arm1 and Arm2, placed in two regions on the opposite sides of LHC Interaction Point 1 (IP1). These regions, called Target Neutral Absorber (TAN), are located at a distance of 141.05 m from IP1, after the dipole magnets that bend the two proton beams. In this position, the two detectors are capable of detecting neutral particles generated from hadronic collisions in $\eta > 8.4$.

The analysis results discussed in this paper were obtained using the LHCf Arm2 detector. This detector consists of two calorimetric towers with different transverse sizes: the *small tower* (25 mm × 25 mm) and the *large tower* (32 mm × 32 mm). Each tower is made of 16 $Gd_2SiO_5$ (GSO) scintillator layers (1 mm thick), interleaved with 22 tungsten (W) plates (7 mm thick), for a total length of about 21 cm, which is equivalent to 44 $X_0$ or 1.6 $\lambda_I$. In addition, 4 xy imaging layers, made of silicon microstrip detectors with a read-out pitch of 160 $\mu$m, are inserted at different depths. In this way, for all particles hitting the detector, it is possible to reconstruct the incident energy (from scintillator layers) and the transverse position (from imaging layers). Considering the reconstruction performances for hadrons between 1 and 6.5 TeV, detection efficiency ranges from about 52% to 72%, energy resolution from 28% to 38%, and position resolution from 300 $\mu$m to 100 $\mu$m [20].

Thanks to the detector design, photons and hadrons are easily separated using the different features of electromagnetic and hadronic showers. However, being unable to distinguish among hadrons, our measurement contains not only neutrons and antineutrons, but also $\Lambda^0$, $K^0_L$ and other neutral and charged hadrons. As described later, this residual background is subtracted at the end of the analysis by the usage of Monte Carlo simulations.

## 3 Experimental data set

The experimental data set analyzed in this paper, relative to p-p collisions at $\sqrt{s} = 13$ TeV, was acquired from 22:32 of June 12th to 1:30 of June 13th 2015 (CEST). This time period corresponds to the LHC Fill 3855, a special low luminosity (3-5 $\times 10^{28}$ cm$^{-2}$s$^{-1}$) and high $\beta^*$ (19 m) fill specifically provided for LHCf operations. In this fill, 29 bunches collided at IP1 with a downward half crossing angle of 145 $\mu$rad. Additionally, 6 and 2 bunches that did not collide at IP1 circulated in the clockwise and counter-clockwise beams, respectively. Given the 0.007–0.012 average number of collisions per bunch crossing and the 15% acceptance of the calorimeter for inelastic collisions, event pile-up at the detector level was estimated to be below 1%, and was therefore neglected in this analysis. Using the instantaneous luminosity measured from the ATLAS experiment [21] and taking into account LHCf data acquisition live time, the recorded integrated luminosity was estimated to be 0.194 nb$^{-1}$.

## 4 Simulation data set

Monte Carlo simulations with the same experimental configuration used for LHC data taking are necessary for four different purposes: estimation of correction factors and systematic uncertainties, validation of the whole analysis procedure, energy spectra unfolding, and data-model comparison. A detailed description of all the simulation data sets, regarding how they were generated, which models were used and which effects were considered, can be found in [18]. Here we simply remind that, depending on the purpose, a given sample is generated taking into account at least one of the following steps: hadronic collision, transport of secondary products from IP1 to TAN, and detector interaction. Cosmos 7.633 [22] and EPICS 9.15 [23] libraries were used for all these simulation steps, except for the samples needed for the final data-model comparison. In this last case, QGSJET II-04, EPOS-LHC, SIBYLL 2.3 and DPMJET 3.06 [24] data sets were simulated using CRMC [25], an interface tool for event generators, whereas PYTHIA 8.212 [26] data set was simulated using its own dedicated interface.

## 5 Analysis

In this section, we present the analysis procedure, divided in four main steps. First, after defining the event selection criteria, we reconstruct the events in the sample and derive the folded energy distributions for each pseudorapidity region (section 5.1). Second, we estimate the correction factors that must be applied to the spectra before and after unfolding (section 5.2). Third, the effect of migration between energy bins is unfolded using a deconvolution

| | Region A | Region B | Region C | Region D | Region E | Region F |
|---|---|---|---|---|---|---|
| $\eta$ | 10.75–$\infty$ | 10.06–10.75 | 9.65–10.06 | 8.99–9.21 | 8.80–8.99 | 8.65–8.80 |
| $\theta$ [$\mu$rad] | 0–42 | 42–85 | 85–128 | 198–249 | 249–298 | 298–347 |
| $\phi$ [°] | 90–270 | 135–215 | 150–200 | 45–70 | 45–70 | 45–70 |

**Table 1**: Definition of the six pseudorapidity regions used in the analysis: for each one, we report the coverage in terms of pseudorapidity $\eta$, scattering angle $\theta$ and azimuthal angle $\phi$.

procedure that takes into account the detector response (section 5.3). Fourth, all necessary systematic uncertainties are evaluated and associated to the unfolded spectra (section 5.4). Finally, these distributions are used to derive our experimental measurements, which are also compared to various generator predictions. This is the topic of the next two sections, where we discuss the results relative to the inclusive differential production cross section (section 6) and to several quantities connected to air shower development (section 7).

### 5.1 Event reconstruction

Apart from small refinements, event reconstruction algorithms and event selection criteria are similar to the ones described in [18]. The incident energy is reconstructed from the total energy deposit in the calorimeter, properly weighting each scintillator layer for its relative sampling step and applying position dependent correction factors. The transverse position is determined by fitting the shower lateral profile reconstructed in imaging layers: during this step, we always look for a single peak in each tower (*singlehit* event), whereas misreconstruction in case of more than a simultaneous hit (*multihit* event) is corrected later. An event is accepted if it satisfies a software trigger condition, defined as a raw energy deposit above 850 MeV in at least three consecutive scintillator layers, which has a good selection efficiency for hadrons with incident energy above 500 GeV. Hadron candidates are then selected using the variable $L_{2D} = L_{90\%} - 0.25 \times L_{20\%}$, where $L_{X\%}$ represents the longitudinal depth where the fraction of the energy deposit respect to the total release in the calorimeter is $X\%$. Finally, after considering the beam center projection on the detector plane, we check if the event is inside one of the six pseudorapidity regions selected for this analysis. Three of these pseudorapidity intervals ($\eta > 10.75$, $8.99 < \eta < 9.21$ and $8.80 < \eta < 8.99$) were already considered in [18], whereas the remaining three ($10.06 < \eta < 10.75$, $9.65 < \eta < 10.06$ and $8.65 < \eta < 8.80$) are added in this work. The six regions superimposed to the detector area are shown in Figure 1, whereas more details on their definition are given in table 1.

### 5.2 Correction factors

Correction factors applied to distributions account for the same effects and amount to the same values described in [18]. Here we shortly discuss them in the same order they are considered on the energy spectra. Note that they are applied before unfolding until *fake events*, and after unfolding since *missed events*. The first correction is due to *beam background*, caused by two different processes: the interaction of primary protons with residual gas in the beam line and the interaction of secondary particles from collisions with the beam

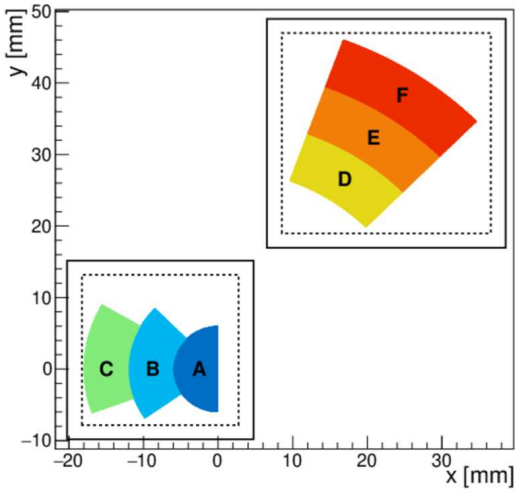


**Figure 1**: Definition of the six pseudorapidity regions used in the analysis. Bottom left and upper right squares respectively correspond to the small and the large tower of the Arm2 detector as seen from IP1. The origin of the reference frame is centered in the beam center projection on the detector plane during LHC Fill 3855. All analysis regions are chosen within a fiducial area (dashed line), which is 2 mm inside the tower edges (solid line).

pipe. The former, estimated using non-crossing bunches, leads to a correction of about -1%, whereas the latter, estimated using dedicated simulations, ranges from 0% to -10%, depending on the energy. The second correction accounts for the limited efficiency (hadron identification) and purity (photon contamination) of *PID selection*. Correction factors, estimated via template fit of the $L_{2D}$ distributions of simulated photons and hadrons to the experimental one, range between -20% and +10%, whereas the uncertainty, obtained from the combination of a dedicated confidence interval fit and different template fit strategies, goes from 1% to 20%. The third correction is due to *multihit events*, which, as described in section 5.1, are not properly reconstructed. Exploiting two simulation samples generated using QGSJET II-04 and EPOS-LHC, we estimated correction factors, given by their average, ranging between -15% and +5%, with an uncertainty, given by half of their deviation, going from 1% to 10%. The fourth correction accounts for *fake events* and *missed events*, *i.e.* the events that, due to detector misreconstructions, are either incorrectly *included in*, or incorrectly *excluded from*, the measured distributions. Corrections factors, estimated employing the same simulation samples and the same computation method just described, range from -1% to -10% for fake events and from +40% to more than +100% for missed events. As expected, missed events are the dominant contribution to correction factors because of the small hadron detection efficiency, which is even more seriously limited at low energy. However, both fake events and missed events do not have a strong dependence on the model used to generate the collisions, so that the systematic uncertainty associated to their correction is negligible respect to the other sources. The last correction is due to *hadron contamination*, *i.e.* the fact that a non-negligible fraction of hadrons reaching the detector are not actually neutrons, but it is not possible to distinguish among them.

Exploiting five simulation samples generated using all the models discussed in Sec.4, we estimated correction factors, given by their average, ranging between -5% and -60%, with an uncertainty, given by their maximum deviation, going from 5% to 20%.

### 5.3 Spectra unfolding

Given the limited hadron energy resolution, we chose to apply spectra unfolding in order to deconvolute our measurements from the detector response. For this purpose, we used the iterative Bayesian method [27], implemented in the RooUnfold package [28]. The best estimation for the final unfolded distributions was obtained choosing a flat prior as initial hypothesis and constructing the response matrix from a single neutron flat energy sample simulated using the DPMJET 3.04 model. In order to estimate the uncertainties due to the deconvolution, the unfolding procedure was repeated several times with different priors, response matrices, or test input spectra. As a general convergence criteria, we decided to stop the iterative method when $\Delta\chi^2$, the $\chi^2$ change between the outputs of two consecutive iterations, was below 1. This threshold was chosen as a compromise between convergence requirements and the number of iterations needed to reach that convergence.

### 5.4 Systematic uncertainties

Systematic uncertainties applied to distributions are due to the same effects and amount to the same values described in [18]. All contributions are assumed to be independent and added in quadrature on the final result. Here we shortly discuss each of them in the same order they are considered on the energy spectra. Note that they are applied before unfolding until *detection efficiency*, and after unfolding since *spectrum unfolding*. While the latter can directly be added to the final distributions, the former must be correctly propagated through the unfolding procedure. The first uncertainty is relative to the *energy scale*, which is known with an error of $\pm 4.5\%$, given by the contributions due to the detector calibration at SPS, the LHC data taking condition and the observed $\pi^0$ mass peak shift. The contribution to the final uncertainty, estimated by shifting the energy scale for the corresponding error and comparing them with the nominal distribution, ranges between 1% and 100%, thus representing the dominant contribution to the systematic uncertainty. The second uncertainty is associated to the *beam center* projection on the detector plane, which was determined by fitting the position distribution of high energy hadrons with a two dimensional function, leading to an error of $\pm 0.3$ mm. The corresponding uncertainty, obtained by shifting the beam center for the corresponding error on the two axes and comparing them with the nominal distribution, is always below 10%. The third uncertainty comes from the *position resolution*, which is not taken into account in the deconvolution in order to simplify the unfolding procedure. Exploiting two simulation samples generated using QGSJET II-04 and EPOS-LHC, we estimated an uncertainty, given by the ratio between the spectra obtained from true and reconstructed position, which is mostly below 20%. The fourth uncertainty is relative to *correction factors* described in Sec.5.2 and it was already discussed there. The fifth uncertainty is associated to the *integrated luminosity* and it was derived from ATLAS measurements for an energy independent value of 1.9%. The sixth uncertainty comes from the *detection efficiency*, which is affected by the error on the hadron-detector interaction cross section at high energy. Comparing the values obtained

for the DPMJET 3.04 model in EPICS to the ones obtained for QGSP_BERT 4.0 model in GEANT4 [29], we estimated an uncertainty, given by the maximum deviation below 6.5 TeV, which amounts to an energy independent value of 6%. The last uncertainty accounts for three different contributions relative to *spectrum unfolding*: method uncertainty, due to the deviation between unfolded spectrum and true distribution, estimated using different generators; prior uncertainty, due to the dependence of the unfolded spectrum on the prior chosen as input of the algorithm, estimated using different priors; algorithm uncertainty, due to the dependence of the unfolded result on the deconvolution algorithm, estimated using different approaches (Bayesian, SVD [30] and TUnfold [31]). All these three contributions are mostly below 20%, except at high energy where they can reach a larger value, especially if the distribution dramatically decreases near the upper edge of the histogram.

## 6 Results

In this section, we present the measurements relative to neutron production and we compare them with model predictions. Distributions are expressed in terms of the inclusive differential production cross section $d\sigma_n/dE$ for six pseudorapidity intervals. In each interval, the distribution is corrected to take into account the limited coverage of the detector in terms of the azimuthal angle. After that, data are compared with generators, using for each model its own inelastic cross section, as reported in [32].

The Arm2 $d\sigma_n/dE$ unfolded distributions are shown in figure 2. The total uncertainty is given by the quadratic sum of all statistical and systematic contributions. The values of the inclusive differential production cross section are also summarized in appendix A. At a first glance, it is interesting to note that all experimental distributions exhibit a peak structure, whose position progressively moves to lower energy as pseudorapidity decreases, from about 5 TeV in $\eta > 10.76$ to about 1.5 TeV in $8.65 < \eta < 8.80$. Furthermore, we found that all these distributions, except the one relative to the most forward region, can be fitted by a very simple function like an asymmetric gaussian, fact that could give a hint on the underlying physical process responsible for neutron production.

Considering the data-model comparison, the largest deviation between model distributions and experimental data is in $\eta > 10.76$, as already noted in [18]. In this region, LHCf measurements indicate a peak structure at around 5 TeV which is not predicted by any generator and, in addition, all models underestimate the total production cross section by at least 20% (QGSJET II-04). No model completely reproduces the experimental measurements even in the other five regions, although deviations are smaller than in $\eta > 10.76$. Depending on the pseudorapidity region, the generator showing the best overall agreement with data is either SIBYLL 2.3 or EPOS-LHC. In $10.06 < \eta < 10.75$, EPOS-LHC reproduces well the peak position but it underestimates neutron production, whereas in $9.65 < \eta < 10.06$ SIBYLL 2.3 reproduces well the peak position but it overestimates neutron production. In the remaining three regions, it is interesting to note that SIBYLL 2.3 is compatible with the experimental measurements in the energy range between 1.5 TeV and 2.5 TeV, where the production peak is located. However, SIBYLL 2.3 is the model showing the best overall agreement with data only in $8.99 < \eta < 9.21$, whereas EPOS-LHC is more consistent with the measured distributions in $8.80 < \eta < 8.99$ and $8.65 < \eta < 8.80$.

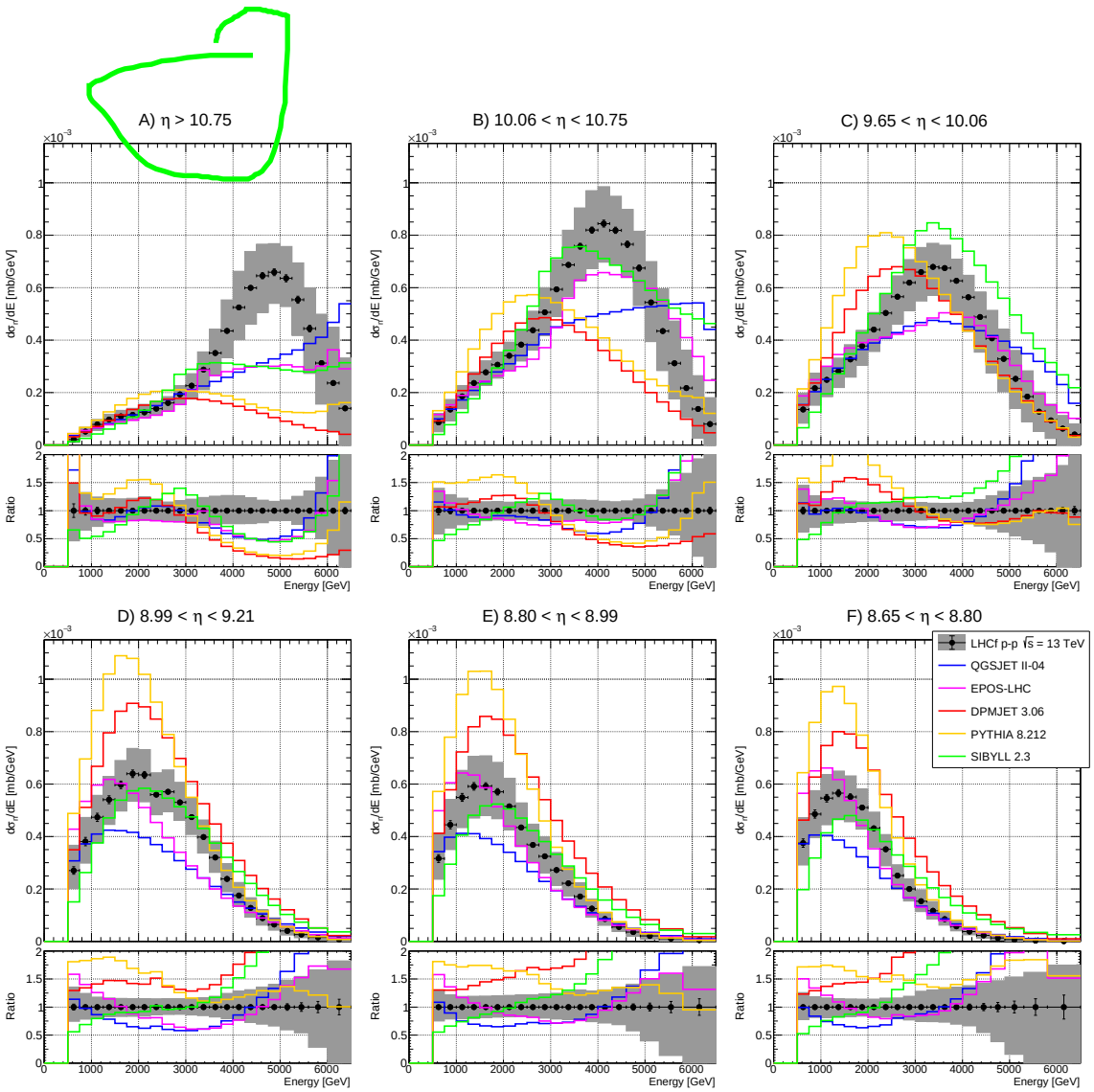


**Figure 2**: Inclusive differential neutron production cross section for p-p collisions at $\sqrt{s} = 13$ TeV, measured using the LHCf Arm2 detector. Black markers represent the experimental data with statistical errors, whereas gray bands represent the quadratic sum of statistical and systematic uncertainties. Colored histograms refer to model predictions at the generator level. For each region, the top plot shows the energy distributions expressed as $\mathrm{d}\sigma_\mathrm{n}/\mathrm{dE}$ and the bottom plot the ratios of these distributions to the experimental results.

## 7 Discussion

The results presented in Sec.6 are interesting by themselves and useful for model tuning. However, in order to test the validity of these generators in the context of cosmic ray measurements, it is better to express our results in terms of quantities that are directly connected to air shower physics. For this reason, in this section we use the distributions shown in Fig.2 to extract three important parameters: energy flow, cross section and average inelasticity of forward neutrons.

The differential energy flow $dE_n/d\eta$ and the differential cross section $d\sigma_n/d\eta$ are expressed as a function of pseudorapidity, *i.e.* associating a point to each of the six regions selected for the analysis. For each region, the corresponding mean pseudorapidity, $\eta$, and pseudorapidity interval, $\Delta\eta$, are given by the average value and the distance of the two extremes, respectively[1]. In a similar way, for each energy bin $i$ of $d\sigma_n/dE$ distribution, the mean energy, $E_i$, and the energy interval, $dE_i$, are given by the average value and the distance of the two extremes, respectively. Thus, $dE_n/d\eta$ and $d\sigma_n/d\eta$ are given by

$$\frac{dE_n}{d\eta} = \frac{1}{\Delta\eta}\frac{1}{\sigma_{ine}}\sum_i \left.\frac{d\sigma_n}{dE}\right|_i E_i dE_i \qquad \text{and} \qquad \frac{d\sigma_n}{d\eta} = \frac{1}{\Delta\eta}\sum_i \left.\frac{d\sigma_n}{dE}\right|_i dE_i$$

where we used the TOTEM measurements of $\sigma_{inel} = (79.5 \pm 1.8)$ mb for the total inelastic cross section (and the corresponding uncertainty) of p-p collisions at $\sqrt{s} = 13$ TeV [33]. Note that these quantities must be corrected to take into account the contribution of neutrons below 500 GeV, which are not included in $d\sigma_n/dE$ distributions because of the limited detection efficiency. Correction factors were estimated exploiting five simulation samples generated using all the models discussed in Sec.4, taking the average as best estimation and the maximum deviation as uncertainty. For $dE_n/d\eta$, corrections are at most 1.5% and absolute uncertainties below 1%, whereas, for $d\sigma_n/d\eta$, corrections are at most 8% and absolute uncertainties below 5%. Another important aspect is how the several sources of uncertainty acting on $d\sigma_n/dE$ contribute to the uncertainty of these two derived quantities. First we assume that all contributions are independent among them, so that they can be added in quadrature. Then we divide the uncertainties in two groups: bin-by-bin independent (only statistical) and bin-by-bin fully-correlated (all systematic). For each bin-by-bin fully-correlated source, its contribution to the final uncertainty is given by the maximum deviation between the quantity derived from the nominal distribution and the one derived from the distributions corresponding to all possible shifts induced by that uncertainty.

Fig.3 and Tab.2 shows the differential energy flow and the differential production cross section measured using the LHCf Arm2 detector. As expected, in both cases all models underestimate these quantities in $\eta > 10.75$, whereas in the other regions the disagreement between generators and data is less serious. In particular, EPOS-LHC is the model showing the best overall agreement with experimental measurements apart from $8.99 < \eta < 9.21$ for $dE_n/d\eta$. QGSJET II-04 is consistent with data in $9.65 < \eta < 10.75$, but underestimates these quantities in $8.65 < \eta < 9.21$, whereas SIBYLL 2.3 reasonably reproduces $d\sigma_n/d\eta$ but strongly overestimates $dE_n/d\eta$. Furthermore, even if data does not cover the region in $9.21 < \eta < 9.65$, experimental measurements seem to indicate that, if $dE_n/d\eta$ has a clear peak as expected by all models except EPOS-LHC, the peak must be located here.

Average inelasticity $\langle 1 - k \rangle$ can be extracted from the elasticity distribution. Here elasticity is defined as $k = 2E/\sqrt{s}$, where $E$ is the energy of the leading particle. The *leading particle* is the particle (not necessarily a baryon) that, on one of the two sides of the collision (let us say $\eta > 0$), carries the largest fraction of the primary proton momentum. Note that, being the detector sensitive to neutrons only, our result refers to the inelasticity of events where the leading particle is a neutron and it differs from the inelasticity that

[1] In case of the most forward region, the upper limit of $\infty$ is limited to 13 for computational reasons. This number was chosen in such a way that more than 95% of the events in this region are below this value.

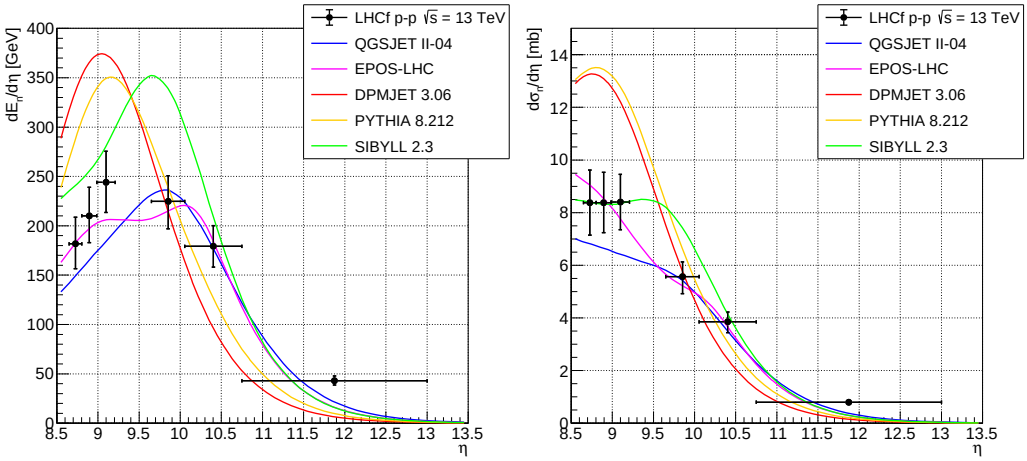


**Figure 3**: Differential energy flow $dE_n/d\eta$ (left) and differential cross section $d\sigma_n/d\eta$ (right) of neutrons generated in p-p collisions at $\sqrt{s} = 13$ TeV, measured using the LHCf Arm2 detector: black markers represent the experimental data with statistical and systematic uncertainties, whereas colored lines refer to model predictions at the generator level.

| | $dE_n/d\eta$ [GeV] | $d\sigma_n/d\eta$ [mb] |
|---|---|---|
| $8.65 < \eta < 8.80$ | $181.8^{+27.0}_{-25.2}$ | $8.38^{+1.24}_{-1.23}$ |
| $8.80 < \eta < 8.99$ | $210.1^{+29.0}_{-27.1}$ | $8.38^{+1.15}_{-1.13}$ |
| $8.99 < \eta < 9.21$ | $244.0^{+31.7}_{-30.4}$ | $8.40^{+1.05}_{-1.05}$ |
| $9.65 < \eta < 10.06$ | $224.7^{+26.1}_{-27.7}$ | $5.57^{+0.56}_{-0.65}$ |
| $10.06 < \eta < 10.75$ | $179.2^{+21.0}_{-21.0}$ | $3.85^{+0.38}_{-0.41}$ |
| $\eta > 10.75$ | $43.0^{+4.8}_{-4.3}$ | $0.80^{+0.08}_{-0.07}$ |

**Table 2**: Differential energy flow $dE_n/d\eta$ and differential cross section $d\sigma_n/d\eta$ of neutrons generated in p-p collisions at $\sqrt{s} = 13$ TeV, measured using the LHCf Arm2 detector. Upper and lower uncertainties are also reported. The values, expressed as a function of $\eta$ interval, are relative to the experimental measurements shown in Fig.3.

we would measure in case we could detect the real leading particle of each event. Using generators, we estimated that: 1) for a given energy bin, the fraction of events where the leading particle is a neutron is about $5 - 35\%$; 2) above half the beam energy, the fraction of neutrons that are leading particle is almost 100%. In order to obtain the elasticity distribution we proceed in the following way. At first we sum the $d\sigma_n/dE$ contributions of all the six regions in a single histogram. Then, we scale the x axis to beam energy and multiply the y axis for bin width, so that the distribution represents the total production cross section $\sigma_n$ as a function of elasticity $k$. At this point we must apply a correction to take into account two different effects: the first one is due to the fact that we want to cover the region $\eta > 0$ but our detector has a limited pseudorapidity coverage; the second one is due to the fact that not all neutrons are leading particles. These two effects are considered together in a single correction factor that was estimated exploiting five simulation samples

generated using all the models discussed in Sec.4, taking the average as best estimation and the maximum deviation as uncertainty. Corrections range between 1% and 70%, whereas absolute uncertainties goes from 5% to 70%. The several sources of uncertainty acting on $d\sigma_n/dE$ contribute to the uncertainty on this distribution in a similar way to what described above, *i.e.* assuming that all contributions are independent each other and dividing them in bin-by-bin independent (only statistical) and bin-by-bin fully-correlated (all systematic) sources. Note that, differently from the previous case, the term *bin* does not refer to the energy bin, but to the pseudorapidity bin, because summation index is on energy, not pseudorapidity. The elasticity distribution cannot directly be used to extract the error on the average inelasticity, because systematic uncertainties are both energy-by-energy and pseudorapidity-by-pseudorapidity correlated. Thus we repeat the entire procedure, but, instead of building a histogram, we simply compute the average as a numerical value, so that both sources of correlation are correctly considered in the estimation of the uncertainty. This value is then corrected to take into account the contribution of neutrons below 500 GeV, in a similar way to what discussed above, leading to a correction factor of $(0.4 \pm 0.4)\%$.

Fig.4 shows the inclusive production cross section as a function of elasticity and the average inelasticity extracted from that distribution, measured using the LHCf Arm2 detector. The contribution to the error bars is dominated by the uncertainty on $d\sigma_n/dE$ for large value of $k$ and by the uncertainty on elasticity correction factors for small value of $k$. As we can see, no generator shows a satisfactory agreement with the experimental measurements in all the elasticity range. In particular, for $0.3 < k < 0.6$, data lays between SIBYLL 2.3 and EPOS-LHC, QGSJET II-04 predictions. Outside this region, the model most consistent with data is SIBYLL 2.3 for $k < 0.3$, $0.6 < k < 0.8$ and EPOS-LHC for $k > 0.8$. The average inelasticity extracted from the elasticity distribution with the method just discussed is $\langle 1 - k \rangle = (0.536^{+0.031}_{-0.037})$. With a value of 0.533, QGSJET II-04 is the only model consistent with our experimental measurement, even if all the remaining models except PYTHIA 8.212 lay just outside the lower or upper error bar. As a final remark, it is important to note that, despite this nice agreement, the elasticity distribution predicted by QGSJET II-04 is very different from the one observed in data.

## 8 Summary

The LHCf experiment measured the inclusive differential production cross section of forward neutrons (+ antineutrons) generated in $\sqrt{s} = 13$ TeV proton-proton collisions. The analysis covers the following six pseudorapidity regions: $\eta > 10.75$, $10.06 < \eta < 10.75$, $9.65 < \eta < 10.06$, $8.99 < \eta < 9.21$, $8.80 < \eta < 8.99$ and $8.65 < \eta < 8.80$. LHCf measurements were compared to the predictions of several hadronic interaction models: QGSJET II-04, EPOS-LHC, SIBYLL 2.3, DPMJET 3.06 and PYTHIA 8.212. All generators dramatically differ from the experimental results in $\eta > 10.75$, whereas at lower pseudorapidity the data-model agreement is better, even if not satisfactory. In this last case, depending on the pseudorapidity region, the generator showing the best overall agreement with data is either SIBYLL 2.3 or EPOS-LHC. From these distributions we derived three quantities directly connected to air shower development: the energy flow, the cross section and the average inelasticity. The first two quantities are well reproduced by EPOS-LHC, apart

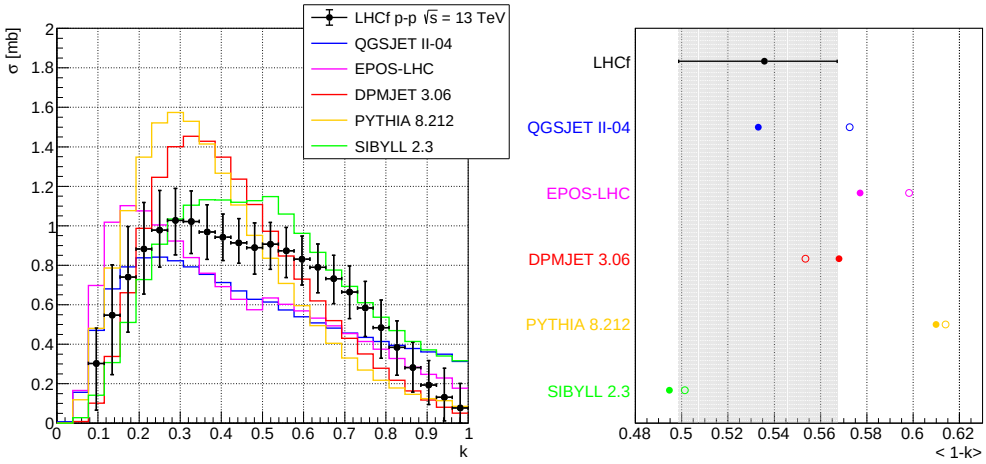


**Figure 4**: Inclusive production cross section as a function of elasticity $k$ (left) and average inelasticity $\langle 1-k \rangle$ extracted from that distribution (right), relative to p-p collisions at $\sqrt{s} =$ 13 TeV. These quantities, measured using the LHCf Arm2 detector, are only relative to the events where the leading particle is a neutron. Black markers represent the experimental data with the quadratic sum of statistical and systematic uncertainties. Solid lines (left) and full circles (right) refer to model predictions at the generator level, obtained using only the events where the leading particle is a neutron. In order to compare this approach to the general case, the average inelasticity obtained using all the events, *i.e.* independently of the nature of the leading particle, is also reported as open circles in the right figure.

from the most forward region, whereas the latter one is consistent only with QGSJET II-04 predictions, even if no generator has a satisfactory agreement with the observed elasticity distribution. Here we want to remark that these are the first measurements of this type at such a high energy and that, given the significant deviation between generators and data, all models would benefit from a tuning that takes into account our results relative to forward neutron production. Furthermore, in the future we will improve this analysis thanks to the common data acquisition that the LHCf and ATLAS experiments had during the operations relative to the data considered here. By exploiting the ATLAS information in the central region, we can tag LHCf triggers on an event-by-event basis, investigating the different mechanisms responsible for neutron production in the forward region [34] and the amount of correlation between central and forward hadron production [35].

## Acknowledgments

We thank the CERN staff and ATLAS Collaboration for their essential contributions to the successful operation of LHCf. We are grateful to S. Ostapchenko for useful comments about QGSJET II-04 generator and to the developers of CRMC interface tool for its implementation. This work was supported by the Japanese Society for the Promotion of Science (JSPS) KAKENHI (Grant Numbers JP26247037, JP23340076) in Japan, by Istituto Nazionale di Fisica Nucleare (INFN) in Italy and by the joint research program of the Institute for Cosmic Ray Research (ICRR), University of Tokyo. This work took advantage of computer resource supplied by ICRR (University of Tokyo), CERN and CNAF (INFN).

## A Table of inclusive differential neutron production cross section

| $\eta > 10.75$ | | $10.06 < \eta < 10.75$ | | $9.65 < \eta < 10.06$ | |
|---|---|---|---|---|---|
| **Energy [GeV]** | **$d\sigma_n/dE$ [mb/GeV]** | **Energy [GeV]** | **$d\sigma_n/dE$ [mb/GeV]** | **Energy [GeV]** | **$d\sigma_n/dE$ [mb/GeV]** |
| 500–750 | $(2.09^{+1.03}_{-1.13}) \times 10^{-5}$ | 500–750 | $(8.66^{+3.45}_{-3.59}) \times 10^{-5}$ | 500–750 | $(1.35^{+0.61}_{-0.52}) \times 10^{-4}$ |
| 750–1000 | $(5.12^{+1.67}_{-1.77}) \times 10^{-5}$ | 750–1000 | $(1.35^{+0.39}_{-0.42}) \times 10^{-4}$ | 750–1000 | $(2.16^{+0.57}_{-0.65}) \times 10^{-4}$ |
| 1000–1250 | $(7.84^{+1.91}_{-2.21}) \times 10^{-5}$ | 1000–1250 | $(1.86^{+0.41}_{-0.47}) \times 10^{-4}$ | 1000–1250 | $(2.49^{+0.48}_{-0.65}) \times 10^{-4}$ |
| 1250–1500 | $(9.75^{+2.03}_{-2.13}) \times 10^{-5}$ | 1250–1500 | $(2.36^{+0.42}_{-0.47}) \times 10^{-4}$ | 1250–1500 | $(2.82^{+0.50}_{-0.63}) \times 10^{-4}$ |
| 1500–1750 | $(1.09^{+0.23}_{-0.21}) \times 10^{-4}$ | 1500–1750 | $(2.77^{+0.45}_{-0.50}) \times 10^{-4}$ | 1500–1750 | $(3.27^{+0.56}_{-0.67}) \times 10^{-4}$ |
| 1750–2000 | $(1.15^{+0.25}_{-0.20}) \times 10^{-4}$ | 1750–2000 | $(3.06^{+0.48}_{-0.51}) \times 10^{-4}$ | 1750–2000 | $(3.78^{+0.60}_{-0.74}) \times 10^{-4}$ |
| 2000–2250 | $(1.24^{+0.31}_{-0.22}) \times 10^{-4}$ | 2000–2250 | $(3.41^{+0.52}_{-0.54}) \times 10^{-4}$ | 2000–2250 | $(4.40^{+0.65}_{-0.84}) \times 10^{-4}$ |
| 2250–2500 | $(1.39^{+0.25}_{-0.24}) \times 10^{-4}$ | 2250–2500 | $(3.82^{+0.60}_{-0.62}) \times 10^{-4}$ | 2250–2500 | $(5.03^{+0.72}_{-0.96}) \times 10^{-4}$ |
| 2500–2750 | $(1.60^{+0.25}_{-0.29}) \times 10^{-4}$ | 2500–2750 | $(4.38^{+0.72}_{-0.76}) \times 10^{-4}$ | 2500–2750 | $(5.66^{+0.79}_{-1.04}) \times 10^{-4}$ |
| 2750–3000 | $(1.93^{+0.34}_{-0.39}) \times 10^{-4}$ | 2750–3000 | $(5.06^{+0.94}_{-0.89}) \times 10^{-4}$ | 2750–3000 | $(6.19^{+0.88}_{-1.07}) \times 10^{-4}$ |
| 3000–3250 | $(2.26^{+0.46}_{-0.51}) \times 10^{-4}$ | 3000–3250 | $(5.93^{+1.14}_{-1.04}) \times 10^{-4}$ | 3000–3250 | $(6.60^{+0.94}_{-1.11}) \times 10^{-4}$ |
| 3250–3500 | $(2.87^{+0.68}_{-0.76}) \times 10^{-4}$ | 3250–3500 | $(6.87^{+1.32}_{-1.21}) \times 10^{-4}$ | 3250–3500 | $(6.79^{+0.90}_{-1.09}) \times 10^{-4}$ |
| 3500–3750 | $(3.51^{+0.90}_{-0.86}) \times 10^{-4}$ | 3500–3750 | $(7.58^{+1.46}_{-1.33}) \times 10^{-4}$ | 3500–3750 | $(6.75^{+0.87}_{-1.19}) \times 10^{-4}$ |
| 3750–4000 | $(4.35^{+1.18}_{-1.02}) \times 10^{-4}$ | 3750–4000 | $(8.19^{+1.50}_{-1.46}) \times 10^{-4}$ | 3750–4000 | $(6.26^{+0.82}_{-1.23}) \times 10^{-4}$ |
| 4000–4250 | $(5.25^{+1.38}_{-1.23}) \times 10^{-4}$ | 4000–4250 | $(8.44^{+1.41}_{-1.47}) \times 10^{-4}$ | 4000–4250 | $(5.63^{+0.84}_{-1.31}) \times 10^{-4}$ |
| 4250–4500 | $(5.99^{+1.39}_{-1.39}) \times 10^{-4}$ | 4250–4500 | $(8.19^{+1.30}_{-1.30}) \times 10^{-4}$ | 4250–4500 | $(4.88^{+0.96}_{-1.34}) \times 10^{-4}$ |
| 4500–4750 | $(6.45^{+1.20}_{-1.40}) \times 10^{-4}$ | 4500–4750 | $(7.65^{+1.33}_{-1.27}) \times 10^{-4}$ | 4500–4750 | $(4.07^{+1.07}_{-1.33}) \times 10^{-4}$ |
| 4750–5000 | $(6.59^{+1.09}_{-1.19}) \times 10^{-4}$ | 4750–5000 | $(6.75^{+1.41}_{-1.43}) \times 10^{-4}$ | 4750–5000 | $(3.28^{+1.13}_{-1.25}) \times 10^{-4}$ |
| 5000–5250 | $(6.36^{+1.21}_{-1.08}) \times 10^{-4}$ | 5000–5250 | $(5.44^{+1.56}_{-1.50}) \times 10^{-4}$ | 5000–5250 | $(2.52^{+1.09}_{-1.13}) \times 10^{-4}$ |
| 5250–5500 | $(5.54^{+1.41}_{-1.36}) \times 10^{-4}$ | 5250–5500 | $(4.34^{+1.61}_{-1.51}) \times 10^{-4}$ | 5250–5500 | $(1.85^{+0.99}_{-0.95}) \times 10^{-4}$ |
| 5500–5750 | $(4.44^{+1.55}_{-1.71}) \times 10^{-4}$ | 5500–5750 | $(3.12^{+1.61}_{-1.36}) \times 10^{-4}$ | 5500–5750 | $(1.27^{+0.75}_{-0.75}) \times 10^{-4}$ |
| 5750–6000 | $(3.12^{+1.86}_{-1.56}) \times 10^{-4}$ | 5750–6000 | $(2.17^{+1.44}_{-1.13}) \times 10^{-4}$ | 5750–6000 | $(9.37^{+6.20}_{-6.89}) \times 10^{-5}$ |
| 6000–6250 | $(2.37^{+2.12}_{-1.86}) \times 10^{-4}$ | 6000–6250 | $(1.37^{+1.27}_{-1.12}) \times 10^{-4}$ | 6000–6250 | $(6.27^{+5.05}_{-6.27}) \times 10^{-5}$ |
| 6250–6500 | $(1.40^{+1.92}_{-1.40}) \times 10^{-4}$ | 6250–6500 | $(8.01^{+10.05}_{-8.01}) \times 10^{-5}$ | 6250–6500 | $(4.03^{+4.01}_{-4.03}) \times 10^{-5}$ |

**Table 3**: Inclusive differential neutron production cross section for p-p collisions at $\sqrt{s} =$ 13 TeV, relative to three of the six regions used in the analysis. These regions are located on the small tower of the LHCf Arm2 detector. Upper and lower uncertainties, expressed as the quadratic sum of statistical and systematics contributions, are also reported.

| $8.99 < \eta < 9.21$ | | $8.80 < \eta < 8.99$ | | $8.65 < \eta < 8.80$ | |
|---|---|---|---|---|---|
| **Energy [GeV]** | **$d\sigma_n/dE$ [mb/GeV]** | **Energy [GeV]** | **$d\sigma_n/dE$ [mb/GeV]** | **Energy [GeV]** | **$d\sigma_n/dE$ [mb/GeV]** |
| 500–750 | $(2.70^{+0.96}_{-0.69}) \times 10^{-4}$ | 500–750 | $(3.16^{+0.96}_{-0.79}) \times 10^{-4}$ | 500–750 | $(3.75^{+0.97}_{-0.84}) \times 10^{-4}$ |
| 750–1000 | $(3.81^{+0.92}_{-0.82}) \times 10^{-4}$ | 750–1000 | $(4.45^{+0.96}_{-0.95}) \times 10^{-4}$ | 750–1000 | $(4.86^{+0.89}_{-0.90}) \times 10^{-4}$ |
| 1000–1250 | $(4.73^{+0.84}_{-0.97}) \times 10^{-4}$ | 1000–1250 | $(5.49^{+1.03}_{-1.15}) \times 10^{-4}$ | 1000–1250 | $(5.46^{+0.90}_{-1.01}) \times 10^{-4}$ |
| 1250–1500 | $(5.40^{+0.89}_{-0.94}) \times 10^{-4}$ | 1250–1500 | $(5.91^{+1.14}_{-1.21}) \times 10^{-4}$ | 1250–1500 | $(5.66^{+0.84}_{-1.02}) \times 10^{-4}$ |
| 1500–1750 | $(5.97^{+0.93}_{-1.00}) \times 10^{-4}$ | 1500–1750 | $(5.91^{+1.16}_{-1.11}) \times 10^{-4}$ | 1500–1750 | $(5.51^{+0.80}_{-0.94}) \times 10^{-4}$ |
| 1750–2000 | $(6.39^{+0.97}_{-1.05}) \times 10^{-4}$ | 1750–2000 | $(5.71^{+1.13}_{-1.03}) \times 10^{-4}$ | 1750–2000 | $(5.10^{+0.72}_{-0.82}) \times 10^{-4}$ |
| 2000–2250 | $(6.35^{+0.96}_{-1.03}) \times 10^{-4}$ | 2000–2250 | $(5.15^{+1.07}_{-0.90}) \times 10^{-4}$ | 2000–2250 | $(4.31^{+0.62}_{-0.72}) \times 10^{-4}$ |
| 2250–2500 | $(5.60^{+0.83}_{-0.77}) \times 10^{-4}$ | 2250–2500 | $(4.35^{+0.94}_{-0.74}) \times 10^{-4}$ | 2250–2500 | $(3.51^{+0.56}_{-0.63}) \times 10^{-4}$ |
| 2500–2750 | $(5.70^{+0.84}_{-0.76}) \times 10^{-4}$ | 2500–2750 | $(3.68^{+0.79}_{-0.67}) \times 10^{-4}$ | 2500–2750 | $(2.51^{+0.41}_{-0.53}) \times 10^{-4}$ |
| 2750–3000 | $(5.30^{+0.77}_{-0.69}) \times 10^{-4}$ | 2750–3000 | $(3.25^{+0.75}_{-0.64}) \times 10^{-4}$ | 2750–3000 | $(2.00^{+0.39}_{-0.46}) \times 10^{-4}$ |
| 3000–3250 | $(4.74^{+0.71}_{-0.67}) \times 10^{-4}$ | 3000–3250 | $(2.72^{+0.67}_{-0.58}) \times 10^{-4}$ | 3000–3250 | $(1.54^{+0.43}_{-0.40}) \times 10^{-4}$ |
| 3250–3500 | $(3.98^{+0.65}_{-0.61}) \times 10^{-4}$ | 3250–3500 | $(2.22^{+0.61}_{-0.49}) \times 10^{-4}$ | 3250–3500 | $(1.17^{+0.36}_{-0.30}) \times 10^{-4}$ |
| 3500–3750 | $(3.20^{+0.62}_{-0.57}) \times 10^{-4}$ | 3500–3750 | $(1.71^{+0.52}_{-0.41}) \times 10^{-4}$ | 3500–3750 | $(8.50^{+2.90}_{-2.30}) \times 10^{-5}$ |
| 3750–4000 | $(2.38^{+0.58}_{-0.49}) \times 10^{-4}$ | 3750–4000 | $(1.26^{+0.36}_{-0.33}) \times 10^{-4}$ | 3750–4000 | $(5.78^{+2.04}_{-1.78}) \times 10^{-5}$ |
| 4000–4250 | $(1.75^{+0.50}_{-0.41}) \times 10^{-4}$ | 4000–4300 | $(8.53^{+2.61}_{-2.43}) \times 10^{-5}$ | 4000–4300 | $(3.76^{+1.43}_{-1.26}) \times 10^{-5}$ |
| 4250–4500 | $(1.28^{+0.39}_{-0.35}) \times 10^{-4}$ | 4300–4600 | $(5.53^{+1.97}_{-1.75}) \times 10^{-5}$ | 4300–4600 | $(2.29^{+0.97}_{-1.04}) \times 10^{-5}$ |
| 4500–4750 | $(8.91^{+3.19}_{-2.73}) \times 10^{-5}$ | 4600–4900 | $(3.59^{+1.47}_{-1.53}) \times 10^{-5}$ | 4600–4900 | $(1.35^{+0.64}_{-0.83}) \times 10^{-5}$ |
| 4750–5000 | $(6.43^{+2.59}_{-2.18}) \times 10^{-5}$ | 4900–5300 | $(2.10^{+1.02}_{-1.27}) \times 10^{-5}$ | 4900–5300 | $(7.22^{+3.87}_{-6.08}) \times 10^{-6}$ |
| 5000–5300 | $(4.05^{+1.91}_{-1.65}) \times 10^{-5}$ | 5300–5800 | $(1.10^{+0.64}_{-0.95}) \times 10^{-5}$ | 5300–5800 | $(3.38^{+2.10}_{-3.38}) \times 10^{-6}$ |
| 5300–5600 | $(2.63^{+1.44}_{-1.22}) \times 10^{-5}$ | 5800–6500 | $(4.89^{+3.53}_{-4.89}) \times 10^{-6}$ | 5800–6500 | $(1.37^{+1.02}_{-1.37}) \times 10^{-6}$ |
| 5600–6000 | $(1.51^{+1.00}_{-1.09}) \times 10^{-5}$ | | | | |
| 6000–6500 | $(7.76^{+6.38}_{-7.76}) \times 10^{-6}$ | | | | |

**Table 4**: Inclusive differential neutron production cross section for p-p collisions at $\sqrt{s} =$ 13 TeV, relative to three of the six regions used in the analysis. These regions are located on the large tower of the LHCf Arm2 detector. Upper and lower uncertainties, expressed as the quadratic sum of statistical and systematics contributions, are also reported.

## References


[1] A. Aab *et al.* [Pierre Auger Collaboration], "The Pierre Auger Cosmic Ray Observatory," Nucl. Instrum. Meth. A **798** (2015) 172 doi:10.1016/j.nima.2015.06.058 [arXiv:1502.01323 [astro-ph.IM]].

[2] M. Fukushima *et al.* [Telescope Array Collaboration], "Telescope array project for extremely high energy cosmic rays," Prog. Theor. Phys. Suppl. **151** (2003) 206-210. doi:10.1143/PTPS.151.206

[3] R. Alves Batista *et al.*, "Open Questions in Cosmic-Ray Research at Ultrahigh Energies," Front. Astron. Space Sci. **6** (2019) 23 doi:10.3389/fspas.2019.00023 [arXiv:1903.06714 [astro-ph.HE]].

[4] R. Ulrich, R. Engel and M. Unger, "Hadronic Multiparticle Production at Ultra-High Energies and Extensive Air Showers," Phys. Rev. D **83** (2011) 054026 doi:10.1103/PhysRevD.83.054026 [arXiv:1010.4310 [hep-ph]].

[5] L. Evans and P. Bryant, "LHC Machine," JINST **3** (2008) S08001. doi:10.1088/1748-0221/3/08/S08001

[6] G. Anelli *et al.* [TOTEM Collaboration], "The TOTEM experiment at the CERN Large Hadron Collider," JINST **3** (2008) S08007. doi:10.1088/1748-0221/3/08/S08007

[7] S. Abdel Khalek *et al.*, "The ALFA Roman Pot Detectors of ATLAS," JINST **11** (2016) no.11, P11013 doi:10.1088/1748-0221/11/11/P11013 [arXiv:1609.00249 [physics.ins-det]].

[8] K. Aamodt *et al.* [ALICE Collaboration], "Charged-particle multiplicity measurement in proton-proton collisions at $\sqrt{s} = 7$ TeV with ALICE at LHC," Eur. Phys. J. C **68** (2010) 345 doi:10.1140/epjc/s10052-010-1350-2 [arXiv:1004.3514 [hep-ex]].

[9] G. Aad *et al.* [ATLAS Collaboration], "Charged-particle multiplicities in pp interactions measured with the ATLAS detector at the LHC," New J. Phys. **13** (2011) 053033 doi:10.1088/1367-2630/13/5/053033 [arXiv:1012.5104 [hep-ex]].

[10] S. Chatrchyan *et al.* [CMS Collaboration], "Study of the Inclusive Production of Charged Pions, Kaons, and Protons in *pp* Collisions at $\sqrt{s} = 0.9$, 2.76, and 7 TeV," Eur. Phys. J. C **72** (2012) 2164 doi:10.1140/epjc/s10052-012-2164-1 [arXiv:1207.4724 [hep-ex]].

[11] T. Csörgö *et al.* [TOTEM Collaboration], "Elastic Scattering and Total Cross-Section in $p + p$ reactions measured by the LHC Experiment TOTEM at $\sqrt{s} = 7$ TeV," Prog. Theor. Phys. Suppl. **193** (2012) 180 doi:10.1143/PTPS.193.180 [arXiv:1204.5689 [hep-ex]].

[12] S. Ostapchenko, "Monte Carlo treatment of hadronic interactions in enhanced Pomeron scheme: I. QGSJET-II model," Phys. Rev. D **83** (2011) 014018 doi:10.1103/PhysRevD.83.014018 [arXiv:1010.1869 [hep-ph]].

[13] T. Pierog, I. Karpenko, J. M. Katzy, E. Yatsenko and K. Werner, "EPOS LHC: Test of collective hadronization with data measured at the CERN Large Hadron Collider," Phys. Rev. C **92** (2015) no.3, 034906 doi:10.1103/PhysRevC.92.034906 [arXiv:1306.0121 [hep-ph]].

[14] F. Riehn, R. Engel, A. Fedynitch, T. K. Gaisser and T. Stanev, "A new version of the event generator Sibyll," PoS ICRC **2015** (2016) 558 doi:10.22323/1.236.0558 [arXiv:1510.00568 [hep-ph]].

[15] A. Aab *et al.* [Pierre Auger Collaboration], "Testing Hadronic Interactions at Ultrahigh Energies with Air Showers Measured by the Pierre Auger Observatory," Phys. Rev. Lett. **117** (2016) no.19, 192001 doi:10.1103/PhysRevLett.117.192001 [arXiv:1610.08509 [hep-ex]].

[16] O. Adriani *et al.* [LHCf Collaboration], "Technical design report of the LHCf experiment: Measurement of photons and neutral pions in the very forward region of LHC," CERN-LHCC-2006-004.

[17] T. Pierog and K. Werner, "Muon Production in Extended Air Shower Simulations," Phys. Rev. Lett. **101** (2008) 171101 doi:10.1103/PhysRevLett.101.171101 [astro-ph/0611311].

[18] O. Adriani *et al.* [LHCf Collaboration], "Measurement of inclusive forward neutron production cross section in proton-proton collisions at $\sqrt{s} = 13$ TeV with the LHCf Arm2 detector," JHEP **1811** (2018) 073 doi:10.1007/JHEP11(2018)073 [arXiv:1808.09877 [hep-ex]].

[19] O. Adriani *et al.* [LHCf Collaboration], "The LHCf detector at the CERN Large Hadron Collider," JINST **3** (2008) S08006. doi:10.1088/1748-0221/3/08/S08006

[20] K. Kawade *et al.* [LHCf Collaboration], "The performance of the LHCf detector for hadronic showers," JINST **9** (2014) P03016 doi:10.1088/1748-0221/9/03/P03016 [arXiv:1312.5950 [physics.ins-det]].

[21] M. Aaboud *et al.* [ATLAS Collaboration], "Luminosity determination in pp collisions at $\sqrt{s} = 8$ TeV using the ATLAS detector at the LHC," Eur. Phys. J. C **76** (2016) no.12, 653 doi:10.1140/epjc/s10052-016-4466-1 [arXiv:1608.03953 [hep-ex]].

[22] K. Kasahara, Cosmos home page, http://cosmos.n.kanagawa-u.ac.jp/cosmosHome/index.html.

[23] K. Kasahara, EPICS home page, http://cosmos.n.kanagawa-u.ac.jp/EPICSHome/index.html.

[24] F. W. Bopp, J. Ranft, R. Engel and S. Roesler, "Antiparticle to Particle Production Ratios in Hadron-Hadron and d-Au Collisions in the DPMJET-III Monte Carlo," Phys. Rev. C **77** (2008) 014904 doi:10.1103/PhysRevC.77.014904 [hep-ph/0505035].

[25] T. Pierog, C. Baus, R. Ulrich, CRMC home page, https://web.ikp.kit.edu/rulrich/crmc.html.

[26] T. Sjöstrand *et al.*, "An Introduction to PYTHIA 8.2," Comput. Phys. Commun. **191** (2015) 159 doi:10.1016/j.cpc.2015.01.024 [arXiv:1410.3012 [hep-ph]].

[27] G. D'Agostini, "A Multidimensional unfolding method based on Bayes' theorem," Nucl. Instrum. Meth. A **362** (1995) 487. doi:10.1016/0168-9002(95)00274-X

[28] T. Adye, RooUnfold home page, http://hepunx.rl.ac.uk/∼adye/software/unfold.

[29] S. Agostinelli *et al.* [GEANT4 Collaboration], "GEANT4: A Simulation toolkit," Nucl. Instrum. Meth. A **506** (2003) 250. doi:10.1016/S0168-9002(03)01368-8

[30] A. Hocker and V. Kartvelishvili, "SVD approach to data unfolding," Nucl. Instrum. Meth. A **372** (1996) 469 doi:10.1016/0168-9002(95)01478-0 [hep-ph/9509307].

[31] S. Schmitt, "TUnfold: an algorithm for correcting migration effects in high energy physics," JINST **7** (2012) T10003 doi:10.1088/1748-0221/7/10/T10003 [arXiv:1205.6201 [physics.data-an]].

[32] O. Adriani *et al.* [LHCf Collaboration], "Measurement of forward photon production cross-section in proton-proton collisions at $\sqrt{s} = 13$ TeV with the LHCf detector," Phys. Lett. B **780** (2018) 233 doi:10.1016/j.physletb.2017.12.050 [arXiv:1703.07678 [hep-ex]].

[33] G. Antchev *et al.* [TOTEM Collaboration], "First measurement of elastic, inelastic and total cross-section at $\sqrt{s} = 13$ TeV by TOTEM and overview of cross-section data at LHC energies," Eur. Phys. J. C **79** (2019) no.2, 103 doi:10.1140/epjc/s10052-019-6567-0 [arXiv:1712.06153 [hep-ex]].

[34] Q. D. Zhou, Y. Itow, H. Menjo and T. Sako, "Monte Carlo study of particle production in diffractive proton-proton collisions at $\sqrt{s} = 13$ TeV with the very forward detector combined with central information," Eur. Phys. J. C **77** (2017) no.4, 212 doi:10.1140/epjc/s10052-017-4788-7 [arXiv:1611.07483 [hep-ex]].

[35] S. Ostapchenko, M. Bleicher, T. Pierog and K. Werner, "Constraining high energy interaction mechanisms by studying forward hadron production at the LHC," Phys. Rev. D **94** (2016) no.11, 114026 doi:10.1103/PhysRevD.94.114026 [arXiv:1608.07791 [hep-ph]].